Chemical Science

ROYAL SOCIETY OF CHEMISTRY

EDGE ARTICLE

View Article Online
View Journal | View Issue

Cite this: *Chem. Sci.*, 2024, **15**, 9591

All publication charges for this article have been paid for by the Royal Society of Chemistry

Received 18th March 2024
Accepted 14th May 2024

DOI: 10.1039/d4sc01799d

rsc.li/chemical-science

Cross-linked $K_{0.5}MnO_2$ nanoflower composites for high rate and low overpotential Li–CO_2 batteries†

Jiawei Wu,‡[ac] Jian Chen,‡[b] Xiaoyang Chen,[b] Yang Liu,*[ab] Zhe Hu,[d] Feijian Lou,*[a] Shulei Chou[e] and Yun Qiao*[ab]

Rechargeable Li–CO_2 batteries are deemed to be attractive energy storage systems, as they can effectively inhale and fix carbon dioxide and possess an extremely high energy density. Unfortunately, the irreversible decomposition of the insoluble and insulating Li_2CO_3 results in awful electrochemical performance and inferior energy efficiency of Li–CO_2 batteries. Furthermore, the low energy efficiency will exacerbate the extra waste of resources. Therefore, it is vital to design novel and efficient catalysts to enhance the battery performance. Herein, a facile, one-step strategy is introduced to design cross-linked, ultrathin $K_{0.5}MnO_2$ nanoflowers combined with CNTs ($K_{0.5}MnO_2$/CNT) as a highly efficient cathode for Li–CO_2 batteries. Impressively, the Li–CO_2 battery based on the $K_{0.5}MnO_2$/CNT cathode achieves a low overpotential (1.05 V) and a high average energy efficiency (87.95%) at a current density of 100 mA g^{-1}. Additionally, the $K_{0.5}MnO_2$/CNT cathode can steadily run for over 100 cycles (overpotential < 1.20 V). Moreover, a low overpotential of 1.47 V can be obtained even at a higher current density of 1000 mA g^{-1}, indicating the superior rate performance of $K_{0.5}MnO_2$/CNT. This strategy offers new insight and guidance for the development of low-cost and high-performance Li–CO_2 batteries.

Introduction

The massive consumption of fossil fuels has led to a surge in carbon dioxide (CO_2) emissions, which has caused a severe greenhouse effect.[1–3] A straightforward strategy to alleviate this concern is converting CO_2 into renewable energy. Using Li–CO_2 batteries has been considered as one of the most promising approaches for sustainable utilization and reduction of CO_2 to produce electrochemical energy.[4–7] Generally, the electrochemical reaction mechanism of Li–CO_2 batteries is based on the following reaction: $4Li + 3CO_2 \leftrightarrow 2Li_2CO_3 + C$ ($E^o = 2.80$ V *versus* Li/Li^+).[8–11] Unfortunately, Li_2CO_3 as the main discharge product is an insoluble and wide bandgap insulator with thermodynamic stability.[12,13] Consequently, the irreversible decomposition of Li_2CO_3 will lead to large polarization, inferior cycle stability, low energy efficiency, and even battery failure, which are the dominant obstacles in the development of high-performance Li–CO_2 batteries.[14–17] In this regard, exploration and fabrication of effective catalysts is a great choice to improve the CO_2 reduction and evolution reaction.

To date, many efforts have been taken to design efficient catalysts with high catalytic activity. Noble metals, such as Ru, Ir and their oxides, have been demonstrated to enable the reversible formation and decomposition of carbonate at low overpotential, and thus can enhance the energy efficiency of Li–CO_2 batteries,[18–21] whereas, their large-scale application in Li–CO_2 batteries is still limited by the high cost and scarcity of noble metals. Notably, transition metal oxides are regarded as attractive candidates. Recently, Wang and co-workers demonstrated a Mn based metal organic framework with catalytic metal centers and porous structure, which can facilitate the complete and efficient decomposition of the nanostructured Li_2CO_3 as well as reducing the charge overpotential.[22] Thus, introducing low-cost Mn as catalytic metal centers is a promising approach to decompose the discharge product of Li_2CO_3.

In particular, MnO_2 materials have emerged as catalysts, which may enhance the reaction dynamics and reduce the overpotentials for Li–CO_2 batteries. Ge *et al.* first introduced Co-interstitial α-MnO_2 nanowires as a cathode for Li–CO_2 batteries, which can deliver a good capacity of 8160 mA h g^{-1} at 100 mA g^{-1}, high efficiency and high energy density.[23] Meanwhile, IrO_2-decorated few-layered δ-MnO_2 was obtained, in which the IrO_2 acts as catalytically active centers for CO_2

[a]*School of Chemistry and Chemical Engineering, Henan Normal University, Xinxiang, Henan 453007, China. E-mail: liuy986@htu.edu.cn; loufeijian@htu.edu.cn*

[b]*School of Environment and Chemical Engineering, Shanghai University, Shanghai 200444, China. E-mail: yunqiao@shu.edu.cn*

[c]*Sinopec Petroleum Engineering Zhongyuan Co. Ltd, Natural Gas Technology Center, Zhengzhou, Henan 450000, China*

[d]*College of Materials Science and Engineering, Shenzhen University, Shenzhen 518055, China*

[e]*Institute for Carbon Neutralization, College of Chemistry and Materials Engineering, Wenzhou University, Wenzhou, Zhejiang 325035, China*

† Electronic supplementary information (ESI) available. See DOI: https://doi.org/10.1039/d4sc01799d

‡ J. Wu and. J. Chen contributed equally to this work.

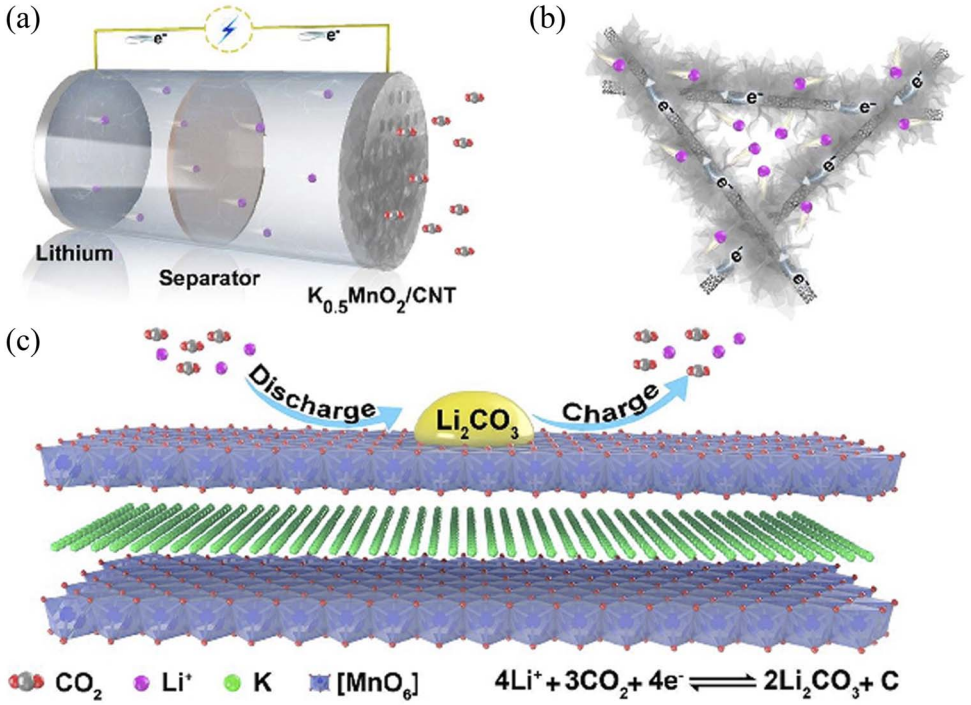

Fig. 1 (a) Schematic diagram of the Li–CO_2 battery with the $K_{0.5}MnO_2$/CNT cathode. (b) The microstructure of $K_{0.5}MnO_2$/CNT and (c) the catalytic mechanism of $K_{0.5}MnO_2$.

reduction, and δ-MnO_2 has a co-catalytic effect for conformal growth of amorphous Li_2CO_3.[24] However, the electrocatalytic performances are still finite for MnO_2 materials as catalytic electrodes in Li–CO_2 batteries. It is commonly recognized that birnessite MnO_2 exhibits the best activity among various MnO_2, while studies on layered MnO_2 as a catalyst in Li–CO_2 batteries are still in their infancy stage.[25–27] Therefore, it is imperative to develop K-birnessite MnO_2 as a feasible catalyst for Li–CO_2 batteries with high performance, taking advantage of the catalytic manganese centers and large interlayer space.

Herein, we adopted a facile method to synthesize ultrathin $K_{0.5}MnO_2$ nanoflowers combined with CNTs ($K_{0.5}MnO_2$/CNT) *via* a hydrothermal process. As a cathode for Li–CO_2 batteries, the $K_{0.5}MnO_2$/CNT electrode exhibits a low overpotential (1.05 V), high average energy efficiency (87.95%) and excellent rate performance (up to 1000 mA g^{-1}). Meanwhile, the cathode can be steadily operated for 100 cycles and the terminal discharge and charge voltages are preserved between 2.72 and 3.92 V. This superb electrochemical performance is ascribed to the outstanding catalytic activity of $K_{0.5}MnO_2$/CNT. Fig. 1 displays the schematic diagram of the typical Li–CO_2 battery with microstructural $K_{0.5}MnO_2$/CNT as a cathode, and the corresponding catalytic reactions for CO_2 reduction and evolution. Of note, the introduction of CNTs can not only improve the electronic conductivity of the composite, but also facilitate the formation of ultrathin $K_{0.5}MnO_2$ nanoflowers with small size and high separation. Simultaneously, the cross-linked ultrathin $K_{0.5}MnO_2$ nanoflowers can effectively shorten the electron/Li^+ transport distances, and also expose ample catalytic active sites. Furthermore, K^+ occupies the interlayer space of $K_{0.5}MnO_2$, which can not only achieve support and charge balance, but also significantly improve the conductivity and the diffusion rate of Li^+. Therefore, $K_{0.5}MnO_2$/CNT can be used as a highly efficient cathode for Li–CO_2 batteries, which is helpful for the realization of ultra-low overpotential, ultra-high energy efficiency, and excellent cycling performance of Li–CO_2 batteries.

Results and discussion

The morphology and microstructure were first characterized through field emission scanning electron microscopy (FE-SEM). Pristine CNTs with an average diameter of about 20–30 nm (Fig. S1†) were first treated with mixed acid, and then the $K_{0.5}MnO_2$/CNT composite was achieved *via* a facile, one-step hydrothermal process. The X-ray diffraction (XRD) patterns of the sample are presented in Fig. S2.† In which, the distinct peaks at 12.5°, 25.2°, 37.3°, and 65.6° in the $K_{0.5}MnO_2$/CNT composite can be well indexed to the (001), (002), ($\bar{1}$11) and (020) planes for monoclinic potassium birnessite (JCPDS No. 80-1098). As shown in Fig. 2a, $K_{0.5}MnO_2$ nanoflowers with diameters of ~200 nm are assembled by ultrathin nanosheets and cover the surface of CNTs, which are cross-linked with each other to form a network void structure. It is of note that the intrinsic voids in the $K_{0.5}MnO_2$/CNT composite with an interconnected network structure can expose more active sites and provide sufficient space for the discharge deposition. The typical transmission electron microscopy image in Fig. 2b clearly discloses that $K_{0.5}MnO_2$ nanoflowers are composed of interconnected nanoflakes alongside CNTs, which can conventionally increase the electronic conductivity of the

composite. The high-resolution transmission electron microscopy (HRTEM) image shows that the thickness of the nanosheets ranges from 2.70 to 3.30 nm (Fig. 2c), which is coincident with 4–5 layers of MnO_2 in the (001) direction with an interplanar spacing of ~0.67 nm. Moreover, the layered structure is further proved by the high-angle-annular dark-field scanning transmission electron microscopy (HAADF-STEM) image in Fig. 2d. The edge-shared [MnO_6] octahedral (bluish violet dots) and K ions (green dots) are alternately distributed between the interlayers, which correspond to 2D layered MnO_2 in the inset of Fig. 2d.[28,29] Two diffraction rings are observed in selected area electron diffraction (SAED) patterns, which can be indexed to the ($\bar{1}11$) and (020) planes of $K_{0.5}MnO_2$ (Fig. 2e). As shown in Fig. 2f, Mn, O, C, and K elements are detected in energy-dispersive X-ray spectra (EDS) of $K_{0.5}MnO_2$/CNT, further confirming the existence of K ions. Moreover, HAADF-STEM mapping images in Fig. 2g–j clearly reveal that K, Mn, and O elements are homogeneously distributed in layered MnO_2 nanoflowers. The presence of K^+ can not only improve the structural stability and charge balance of $K_{0.5}MnO_2$, but also boost the catalytic activity of the electrode.[30] The existence of carbon further confirms that $K_{0.5}MnO_2$ nanoflowers cover the CNTs substrate (Fig. 2k).

Inductively coupled plasma (ICP) analysis was used to investigate the chemical composition of $K_{0.5}MnO_2$/CNT, where the K/Mn molar ratio in $K_{0.5}MnO_2$/CNT is about 0.5/1.0 (Table S1†). Therefore, the molecular formula of $K_{0.5}MnO_2$/CNT can be identified as $K_{0.5}MnO_2$. The thermogravimetric result reveals that the proportion of CNTs in the $K_{0.5}MnO_2$/CNT composite is 16.0% (Fig. S3†). The full X-ray photoelectron spectrum (XPS) of $K_{0.5}MnO_2$/CNT shows distinct characteristic peaks of K, Mn, O and C elements, further indicating the presence of $K_{0.5}MnO_2$ and CNTs (Fig. S4†). In Fig. S5a,† the high-resolution C 1s XPS spectrum can be deconvoluted into three peaks centered at 284.7, 285.5 and 286.8 eV, which can be ascribed to non-oxygenated ring carbon (C–C), C–N and the C–O bonds, respectively.[31–33] Fig. S5b† shows the high-resolution XPS spectrum of Mn 2p; the two peaks at 654.2 and 642.4 eV correspond to the binding energy of Mn $2p_{1/2}$ and Mn $2p_{3/2}$ for $K_{0.5}MnO_2$, respectively. Their spin-energy separation is 11.8 eV, consistent with a previous report.[27] Furthermore, the spectrum of Mn 2p can be resolved into three peaks, confirming the existence of a mixed-valence state of Mn^{4+} (642.5 eV) and Mn^{3+} (644.9 and 654.1 eV) ions in the MnO_6 subunits.[34,35] The high-resolution XPS spectra of Mn 3s exhibit a splitting of the doublet, because of the parallel spin coupling of 3s and 3d electrons during the photoelectron ejection (Fig. S5c†).[36,37] The energy difference of 4.7 V among the two peaks is attributed to the existence of Mn^{4+}. These mixed-valence states of Mn could enhance the catalytic performance of MnO_2 with different oxide species. As shown in Fig. S5d,† the O 1s spectra display three fitted peaks at 529.9, 531.5 and 532.8 eV, which are assigned to the Mn–O–Mn, Mn–O–H, and H–

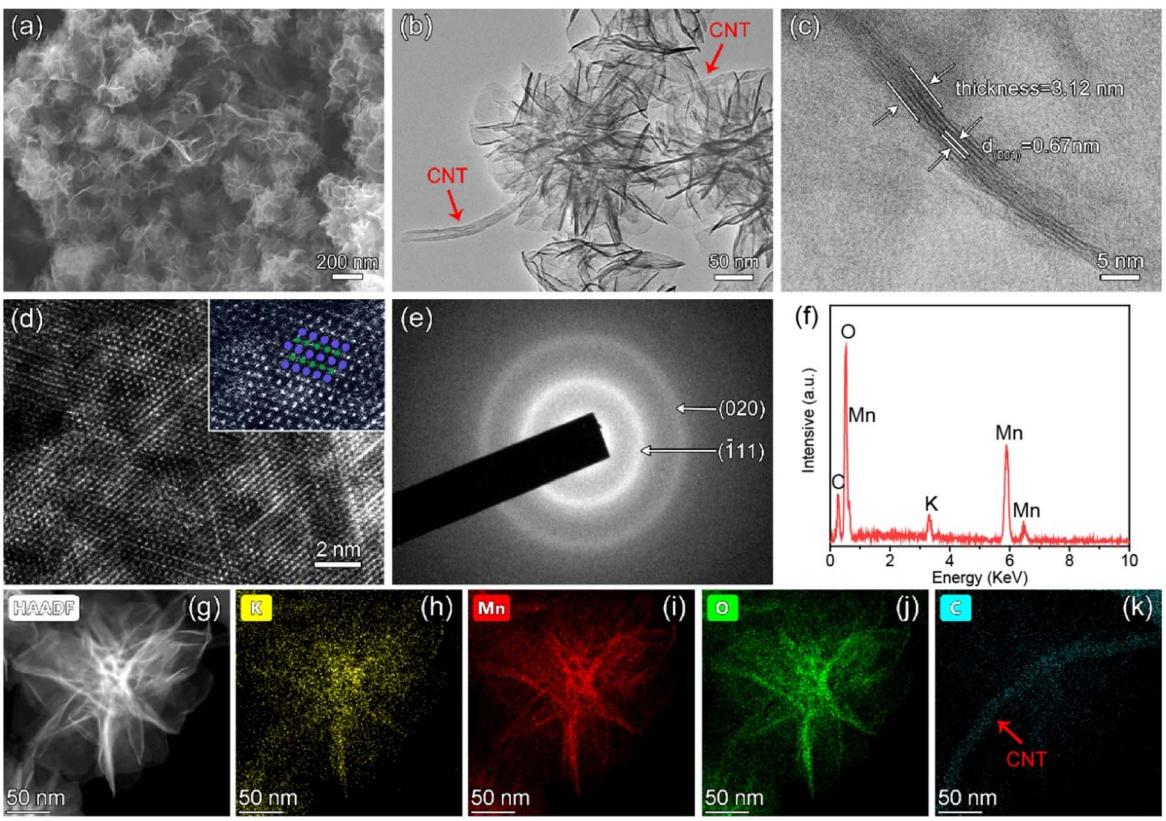

Fig. 2 (a) SEM, (b) TEM, (c) HRTEM, and (d) high-magnification HAADF-STEM images of $K_{0.5}MnO_2$/CNT (inset of Fig. 2d: bluish violet dots stand for [MnO_6] and green dots represent K^+). (e) SAED patterns and (f) EDS spectrum of $K_{0.5}MnO_2$/CNT. (g–k) HAADF-STEM image and the corresponding EDS elemental mapping results of $K_{0.5}MnO_2$/CNT.

O–H (adsorbed water) bonds, respectively.[38] These results prove the successful synthesis of K-birnessite-type MnO_2/CNT.

To evaluate the electrochemical behavior of the $K_{0.5}MnO_2$/CNT cathode in Li–CO_2 batteries, the cyclic voltammetry (CV) measurement was first carried out between 2.0 and 4.5 V at a scan rate of 0.2 mV s^{-1}. As shown in Fig. 3a, the $K_{0.5}MnO_2$/CNT cathode displays an obvious cathodic peak at 2.98 V, indicating the CO_2 reduction reaction. In contrast, none of the significant peaks are found for the CNT cathode. Upon the anodic scan, the $K_{0.5}MnO_2$/CNT cathode exhibits a significantly lower onset potential (≈3.0 V) than that of the CNT cathode (≈3.4 V). The stronger oxidation peak at 3.95 V for the $K_{0.5}MnO_2$/CNT cathode can be ascribed to the CO_2 evolution reaction (CO_2ER) with high activity, implying the remarkably boosted kinetic reaction of Li_2CO_3 decomposition, Li^+ and CO_2 transport. Of note, the $K_{0.5}MnO_2$/CNT cathode also endows the larger integral area and higher peak intensity in the CV curves than that of the CNT cathode, suggesting that the synergistic effect between $K_{0.5}MnO_2$ and CNTs significantly improves the catalytic activity of the CO_2 reduction reaction (CO_2RR) and CO_2ER. Subsequently, deep discharge/charge tests of Li–CO_2 cells with $K_{0.5}MnO_2$/CNT and CNTs as cathodes were also carried out at 100 mA g^{-1} between 2.0 and 4.5 V (Fig. S6†). During the discharge process, the CNT cathode delivers a discharge capacity of 5191 mA h g^{-1}. It is noteworthy that the $K_{0.5}MnO_2$/CNT cathode achieves an increased discharge capacity of 13 408 mA h g^{-1}, which is 2.58 times that of the CNT cathode. Upon the recharge process, the $K_{0.5}MnO_2$/CNT cathode delivers a charge capacity of 14 267 mA h g^{-1}, which is significantly higher than that of the CNT cathode (3926 mA h g^{-1}). The charge capacity is larger than the discharge capacity of the $K_{0.5}MnO_2$/CNT cathode, which can be assigned to minor side reactions during the deep charge and discharge processes. On the basis of the above evidence, the $K_{0.5}MnO_2$/CNT nanoflowers as a catalyst play a significant role in enhancing the electrocatalytic activity of the cathode.

Fig. 3b shows the first discharge–charge curves of $K_{0.5}MnO_2$/CNT and CNT cathodes at 100 mA g^{-1} with a capacity limited to 1000 mA h g^{-1}. The first discharge and charge terminal voltages are 2.86 and 3.91 V, respectively. The corresponding overpotential is as low as 1.05 V, while the overpotential for the CNT electrode is up to 1.84 V, consistent with the CV results. The

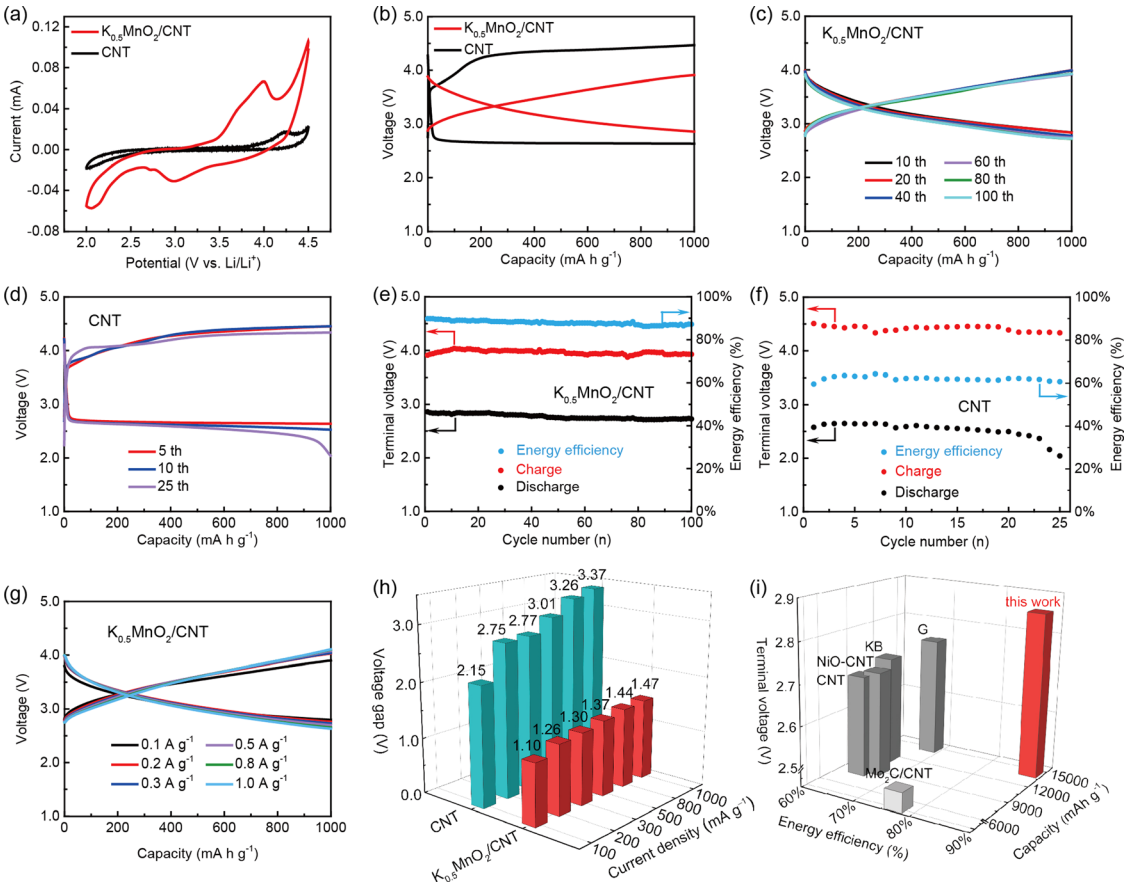

Fig. 3 The electrochemical performance of the cathodes in Li–CO_2 batteries. (a) CV curves of the $K_{0.5}MnO_2$/CNT and CNT electrodes at a scan rate of 0.2 mV s^{-1}. (b) The first discharge/charge curves for $K_{0.5}MnO_2$/CNT and CNT electrodes at 0.1 A g^{-1} with a cut-off capacity of 1000 mA h g^{-1}. (c and d) Discharge/charge profiles of (c) $K_{0.5}MnO_2$/CNT and (d) CNT cathodes at various cycles at a current density of 0.1 A g^{-1}. (e and f) The corresponding terminal discharge/charge voltages and energy efficiencies *versus* cycle number for (e) $K_{0.5}MnO_2$/CNT and (f) CNT cathodes in Li–CO_2 batteries. (g) The charge/discharge profiles of the $K_{0.5}MnO_2$/CNT electrode at various current densities. (h) The overpotential comparison of the two cathodes at different current densities. (i) The performance comparison of $K_{0.5}MnO_2$/CNT with reported cathodes in terms of energy efficiency, full discharge capacity and terminal voltage.

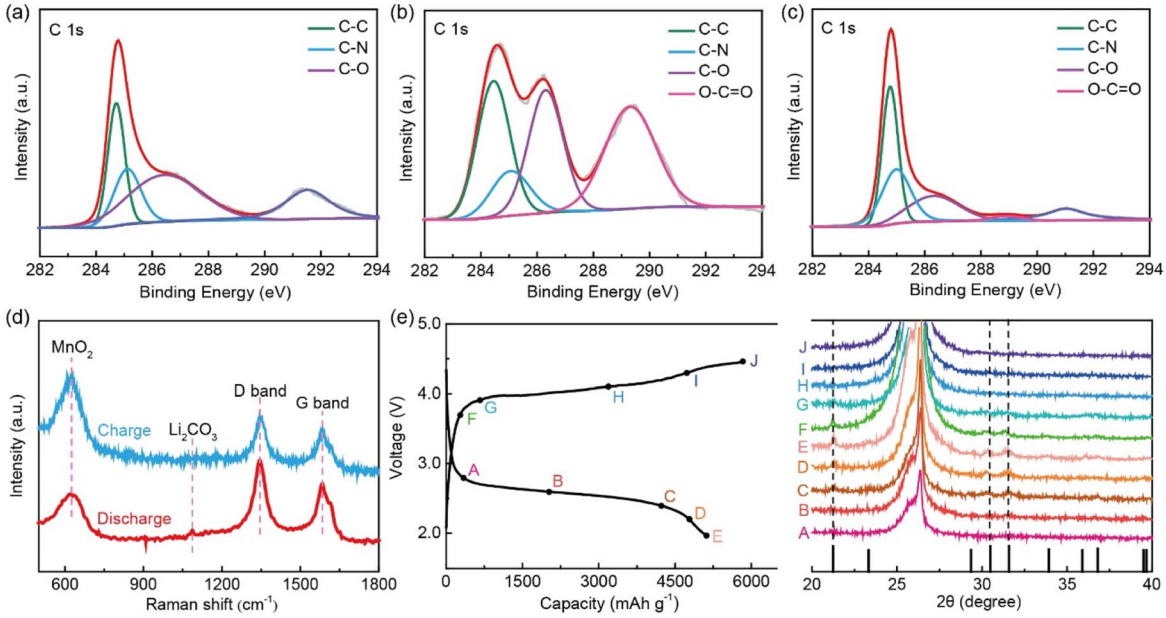

Fig. 4 XPS spectra of C 1s for the $K_{0.5}MnO_2$/CNT based cathodes: (a) pristine, (b) discharged, and (c) recharged, respectively. (d) Raman spectra. (e) XRD patterns of the $K_{0.5}MnO_2$/CNT cathode at different discharge and charge states (right) and the corresponding discharge/charge curves (left) at 100 mA g^{-1}.

subsequent discharge/charge profiles at various cycles prove that the Li–CO_2 battery with $K_{0.5}MnO_2$/CNT as the cathode can be steadily operated over 100 cycles (Fig. 3c). More importantly, the terminal discharge and charge voltages are maintained between 2.72 and 3.92 V with a minimal overpotential of 1.20 V (Fig. 3e). In contrast, the overpotential for the CNT cathode is up to 1.80 V with an inferior energy efficiency of about 60% and the battery can only run for 25 cycles (Fig. 3d and f).

It is worth mentioning that the average energy efficiency for the $K_{0.5}MnO_2$/CNT cathode is as high as 87.95%, which is higher than that of most reported Li–CO_2 batteries (60–80%).[39–43] These results demonstrate that $K_{0.5}MnO_2$/CNT as a cathode exhibits an incredible electrochemical performance with low overpotential, high energy efficiency and excellent cycling stability. To the best of our knowledge, the $K_{0.5}MnO_2$/CNT cathode delivers the best electrochemical performance among the non-previous catalysts for Li–CO_2 batteries reported to date. Fig. 3g shows the charge/discharge curves of Li–CO_2 batteries with the $K_{0.5}MnO_2$/CNT cathode at various current densities. The battery maintains stable discharge and charge plateaus without significant change from 0.1 to 1.0 A g^{-1}, implying its superior rate performance. The overpotentials of the Li–CO_2 battery based on the $K_{0.5}MnO_2$/CNT cathode are 1.10, 1.26, 1.30, 1.37, 1.44, and 1.47 V at current densities of 0.1, 0.2, 0.3, 0.5, 0.8, and 1.0 A g^{-1}, respectively. It is noteworthy that the terminal discharge and charge voltages are stable at 2.64 and 4.11 V, respectively, even when the current density is up to 1.0 A g^{-1}, implying its outstanding rate performance. Concurrently, the decomposition of electrolyte and other side reactions can be effectively avoided due to its low terminal charge voltage.[44,45] It can be intuitively observed that the battery with the $K_{0.5}MnO_2$/CNT cathode displays much lower overpotentials than that with CNTs as the cathode at various current densities (Fig. 3h and S7†). The electrochemical impedance spectroscopy (EIS) tests were performed for $K_{0.5}MnO_2$/CNT and CNT cathodes after the first discharge and charge processes, as shown in Fig. S8.† It can be seen that the charge transfer resistance (R_{ct}) value for $K_{0.5}MnO_2$/CNT after charge is smaller than that of the value after discharge, indicating that $K_{0.5}MnO_2$/CNT delivers a superior catalytic activity in promoting the decomposition of Li_2CO_3. Furthermore, the $K_{0.5}MnO_2$/CNT cathode also delivers evidently smaller R_{ct} values than that of CNTs, suggesting that the synergistic effect between $K_{0.5}MnO_2$ and CNTs can expose ample catalytically active sites, shorten the electron/Li^+ transport distances and facilitate Li_2CO_3 nucleation and decomposition.

In the development of Li–CO_2 batteries, the short cycle life, large overpotential, poor rate performance and inferior energy efficiency are the most urgent and tricky troubles to be solved before commercial application in the future. However, it is also a great challenge to completely solve the above problems. Fortunately, the as-synthesized $K_{0.5}MnO_2$/CNT catalyst can substantially overcome those obstacles. For a more intuitive observation, we compare the electrochemical performance of the $K_{0.5}MnO_2$/CNT cathode with other current reports (Fig. 3i). Besides, the more systematic and detailed comparison is available in Table S2.† Attractively, the Li–CO_2 battery with the $K_{0.5}MnO_2$/CNT cathode presents the overwhelming superiority in the voltage gap, energy efficiency and full discharge capacity. In consequence, $K_{0.5}MnO_2$/CNT is a promising candidate to convert CO_2 into electrical energy using aprotic Li–CO_2 batteries.

To further probe the electrochemical reaction process and mechanism upon the charge–discharge processes, *ex situ*

measurements were performed, such as XPS, Raman and XRD. The deconvoluted C 1s spectra for the $K_{0.5}MnO_2$/CNT cathode at different stages are shown in Fig. 4a–c. Compared with the original cathode (Fig. 4a), the high-resolution C 1s XPS spectra of the fully discharged cathode exhibit a distinct peak at 289.3 eV related to the O–C=O bond in Li_2CO_3 (Fig. 4b). The peak at 291.2 eV for the pristine cathode is attributed to the C–F bond in the PVDF binder. After the discharge process, the peak disappears, as the nucleation of Li_2CO_3 covers the cathode surface, whereas, a relatively smaller peak at ~291.0 eV reappears after the charge process. It is worth noting that the reversible generation and disappearance of Li_2CO_3 after discharge and charge processes indicate that the $K_{0.5}MnO_2$/CNT cathode possesses excellent catalytic reversibility and activity (Fig. 4b and c). These results are further verified by Raman spectroscopy, as shown in Fig. 4d. The Raman peak near 631 cm^{-1} corresponds to the Mn–O bond in the K-birnessite-type MnO_2, indicating the stability of $K_{0.5}MnO_2$/CNT during the cycling process. Additionally, the two main peaks detected at 1346 and 1586 cm^{-1} are attributed to the D and G bands of the CNT, respectively. Importantly, the characteristic peak at 1087 cm^{-1} corresponding to Li_2CO_3 emerges after the discharge process, and it disappears after a recharge process. The *ex situ* XRD patterns of the $K_{0.5}MnO_2$/CNT electrode at different states were recorded to further reveal the electrochemical reaction process and mechanism (Fig. 4e). The intensity of three additional peaks at 21.2°, 30.5° and 31.6° is gradually enhanced in the discharge process, which are attributed to the (110), (202) and (002) peaks of Li_2CO_3 (JCPDS No. 09–0359). Subsequently, these peaks disappear after the charge process, indicating the complete decomposition of Li_2CO_3. These results demonstrate that $K_{0.5}MnO_2$/CNT as the cathode is a promising candidate to propel the reversible reduction and evolution of carbon dioxide.

Density functional theory (DFT) calculations have been conducted to reveal the relationship between the structure and performance. The configurations of graphene and graphene/MnO_2 heterostructures are shown in Fig. 5a and b, respectively.

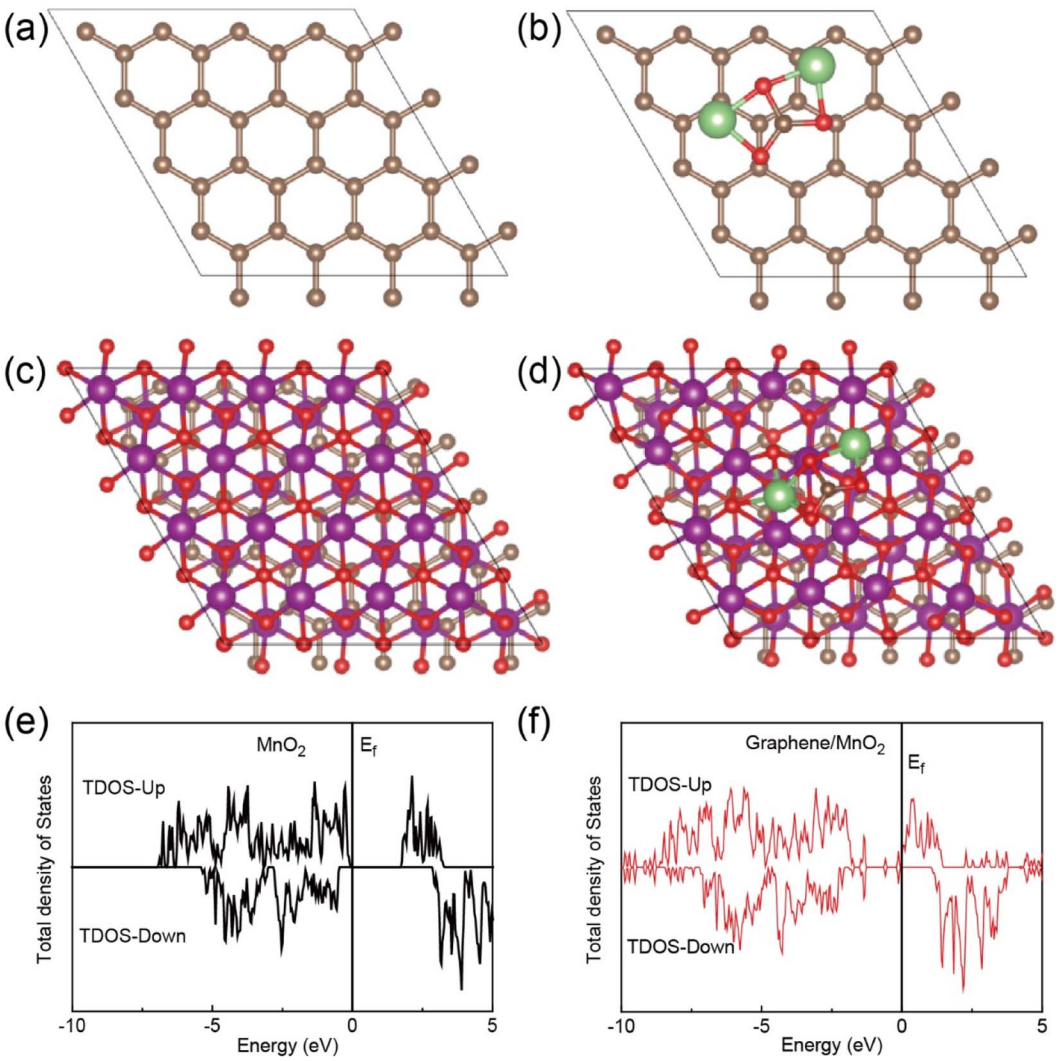

Fig. 5 The configurations of (a) graphene and (b) graphene/MnO_2 heterostructures and the corresponding configurations of Li_2CO_3 adsorption on (c) graphene and (d) graphene/MnO_2 heterostructures. The total density of states for (e) MnO_2 and (f) graphene/MnO_2.

The capability of Li_2CO_3 adsorption was also evaluated. The binding energies with Li_2CO_3 are −0.15 eV for the graphene layer (Fig. 5c) and −2.65 eV for the heterostructure (Fig. 5d), indicating the strong interaction between Li_2CO_3 and the heterostructure. Moreover, pure MnO_2 possesses a band gap, and the heterostructure demonstrates no band gap in reverse, indicating improved electrical conductivity according to the density of state results (Fig. 5e and f).

Conclusions

In summary, we successfully designed a $K_{0.5}MnO_2$/CNT composite as a cathode for Li–CO_2 batteries. Benefiting from the excellent catalytic activity of $K_{0.5}MnO_2$/CNT, the as-assembled Li–CO_2 battery achieves a low overpotential of 1.05 V at a current density of 100 mA g^{-1}. Meanwhile, the $K_{0.5}MnO_2$/CNT cathode can be stably operated over 100 cycles in the voltage window of 2.72–3.92 V with a high average energy efficiency (87.95%). In addition, the $K_{0.5}MnO_2$/CNT cathode still displays a low overpotential of 1.47 V even though the current density is increased to 1.0 A g^{-1}, indicating its superior rate performance for CO_2 reduction and evolution reactions. This work affords an outstanding strategy for designing cheap and efficient catalysts, and the $K_{0.5}MnO_2$/CNT cathode promises to be a promising candidate for further commercial application in Li–CO_2 batteries.

Data availability

Data will be made available on request.

Author contributions

Y. L., F.-J. L. and Y. Q. proposed the concept and supervised the work; J-W. W. and J. C. designed the experiments and wrote the paper; Z. H. and S-L. C. contributed to the discussion and provided suggestions. X-Y. C. helped to analyze the data. All authors have discussed the results, drafted the manuscript and approved the final version of the manuscript.

Conflicts of interest

There are no conflicts to declare.

Acknowledgements

J. Wu and J. Chen contributed equally to this work. This work was supported by the National Natural Science Foundation of China (grant no. U1904187), Natural Science Foundation of Henan for Excellent Young Scholars (no. 202300410223), and the Innovative Research Team of High-Level Local Universities in Shanghai.

Notes and references

1 Y. Yang, S. Louisia, S. Yu, J. Jin, I. Roh, C. Chen, M. V. Fonseca Guzman, J. Feijóo, P.-C. Chen, H. Wang, C. J. Pollock, X. Huang, Y.-T. Shao, C. Wang, D. A. Muller, H. D. Abruña and P. Yang, *Nature*, 2023, **614**, 262–269.
2 M. T. Dunstan, F. Donat, A. H. Bork, C. P. Grey and C. R. Müller, *Chem. Rev.*, 2021, **121**, 12681–12745.
3 S. Ren, D. Joulié, D. Salvatore, K. Torbensen, M. Wang, M. Robert and C. P. Berlinguette, *Science*, 2019, **365**, 367–369.
4 L. Fan, H. Shen, D. Ji, Y. Xing, L. Tao, Q. Sun and S. Guo, *Adv. Mater.*, 2022, **34**, e2204134.
5 K. Zhang, J. Li, W. Zhai, C. Li, Z. Zhu, X. Kang, M. Liao, L. Ye, T. Kong, C. Wang, Y. Zhao, P. Chen, Y. Gao, B. Wang and H. Peng, *Angew. Chem., Int. Ed.*, 2022, **61**, 2201718.
6 B. Chen, D. Wang, J. Tan, Y. Liu, M. Jiao, B. Liu, N. Zhao, X. Zou, G. Zhou and H.-M. Cheng, *J. Am. Chem. Soc.*, 2022, **144**, 3106–3116.
7 X. Sun, X. Mu, W. Zheng, L. Wang, S. Yang, C. Sheng, H. Pan, W. Li, C.-H. Li, P. He and H. Zhou, *Nat. Commun.*, 2023, **14**, 536.
8 Z. Hu, Y. Xie, D. Yu, Q. Liu, L. Zhou, K. Zhang, P. Li, F. Hu, L. Li, S. Chou and S. Peng, *ACS Nano*, 2021, **15**, 8407–8417.
9 F. Ye, L. Gong, Y. Long, S. N. Talapaneni, L. Zhang, Y. Xiao, D. Liu, C. Hu and L. Dai, *Adv. Energy Mater.*, 2021, **11**, 2101390.
10 J. Chen, X.-Y. Chen, Y. Liu, Y. Qiao, S.-Y. Guan, L. Li and S.-L. Chou, *Energy Environ. Sci.*, 2023, **16**, 792–829.
11 J. Zou, G. Liang, F. Zhang, S. Zhang, K. Davey and Z. Guo, *Adv. Mater.*, 2023, **35**, 2210671.
12 Q. Deng, Y. Yang, S. Qu, W. Wang, Y. Zhang, X. Ma, W. Yan and Y. Zhang, *Energy Storage Mater.*, 2021, **42**, 484–492.
13 F. Wang, Y. Li, X. Xia, W. Cai, Q. Chen and M. Chen, *Adv. Energy Mater.*, 2021, **11**, 2100667.
14 Z. Cheng, Y. Fang, Y. Yang, H. Zhang, Z. Fan, J. Zhang, S. Xiang, B. Chen and Z. Zhang, *Angew. Chem., Int. Ed.*, 2023, **62**, e202311480.
15 J. Lin, J. Ding, H. Wang, X. Yang, X. Zheng, Z. Huang, W. Song, J. Ding, X. Han and W. Hu, *Adv. Mater.*, 2022, **32**, 2200559.
16 Y. Xu, H. Gong, L. Song, Y. Kong, C. Jiang, H. Xue, P. Li, X. Huang, J. He and T. Wang, *Mater. Today Energy*, 2022, **1**, 100967.
17 C. Guo, F. Zhang, X. Han, L. Zhang, Q. Hou, L. Gong, J. Wang, Z. Xia, J. Hao and K. Xie, *Adv. Mater.*, 2023, **35**, 2302325.
18 H. Xue, H. Gong, X. Lu, B. Gao, T. Wang, J. He, Y. Yamauchi, T. Sasaki and R. Ma, *Adv. Energy Mater.*, 2021, **11**, 2101630.
19 Y. Xing, Y. Yang, D. Li, M. Luo, N. Chen, Y. Ye, J. Qian, L. Li, D. Yang, F. Wu, R. Chen and S. Guo, *Adv. Mater.*, 2018, **30**, 1803124.
20 Y. Qiao, S. Xu, Y. Liu, J. Dai, H. Xie, Y. Yao, X. Mu, C. Chen, D. J. Kline, E. M. Hitz, B. Liu, J. Song, P. He, M. R. Zachariah and L. Hu, *Energy Environ. Sci.*, 2019, **12**, 1100–1107.
21 Y. Ding, Y. Li and Z.-S. Wu, *Battery Energy*, 2023, **2**, 20220014.
22 S. Li, Y. Dong, J. Zhou, Y. Liu, J. Wang, X. Gao, Y. Han, P. Qi and B. Wang, *Energy Environ. Sci.*, 2018, **11**, 1318–1325.
23 B. Ge, Y. Sun, J. Guo, X. Yan, C. Fernandez and Q. Peng, *Small*, 2019, **15**, 1902220.
24 Y. Mao, C. Tang, Z. Tang, J. Xie, Z. Chen, J. Tu, G. Cao and X. Zhao, *Energy Storage Mater.*, 2019, **18**, 405–413.

25 Q. Liu, Z. Hu, L. Li, W. Li, C. Zou, H. Jin, S. Wang and S.-L. Chou, *ACS Appl. Mater. Interfaces*, 2021, **13**, 16585–16593.
26 X. Chen, J. Chen, Y. Qiao, Y. Gao, S. Fan, Y. Liu, L. Li, Y. Liu and S. Chou, *Chem. Sci.*, 2024, **15**, 2473–2479.
27 X. Chen, J. Chen, Y. Liu, Y. Liu, Y. Gao, S. Fan, X. He, X. Liu, C. Shen, Y. Jiang, L. Li, Y. Qiao and S. Chou, *ACS Appl. Mater. Interfaces*, 2023, **15**, 28106–28115.
28 V. B. R. Boppana, S. Yusuf, G. S. Hutchings and F. Jiao, *Adv. Funct. Mater.*, 2013, **23**, 878–884.
29 W. Lv, J. Meng, Y. Li, W. Yang, Y. Tian, X. Lyu, C. Duan, X. Ma and Y. Wu, *Nano Energy*, 2022, **98**, 107274.
30 Y. Liu, W. Zong, H. Zhou, D. Wang, R. Cao, J. Zhan, L. Liu and B. W.-L. Jang, *Catal. Sci. Technol.*, 2018, **8**, 5344–5358.
31 J. Liu, Y. Zhang, L. Zhang, F. Xie, A. Vasileff and S.-Z. Qiao, *Adv. Mater.*, 2019, **31**, 1901261.
32 X. Li, J. Zhang, G. Qi, J. Cheng and B. Wang, *Energy Storage Mater.*, 2021, **35**, 148–156.
33 K. Lv, D. Wan, R. Pan, W. Suo and Y. Zhu, *Carbon Neutralization*, 2022, **1**, 189–197.
34 Y. Liu, Y. Qiao, X. Lou, X. Zhang, W. Zhang and Y. Huang, *ACS Appl. Mater. Interfaces*, 2016, **8**, 14564–14571.
35 D. Banerjee and H. W. Nesbitt, *Geochim. Cosmochim. Acta*, 1999, **63**, 3025–3038.
36 Y. Liu, Y. Qiao, W. Zhang, H. Wang, K. Chen, H. Zhu, Z. Li and Y. Huang, *J. Mater. Chem. A*, 2015, **3**, 7780–7785.
37 Z. Zhuo, K. Dai, R. Qiao, R. Wang, J. Wu, Y. Liu, J. Peng, L. Chen, Y.-d. Chuang, F. Pan, Z.-x. Shen, G. Liu, H. Li, T. P. Devereaux and W. Yang, *Joule*, 2021, **5**, 975–997.
38 M. Chigane and M. Ishikawa, *J. Electrochem. Soc.*, 2000, **147**, 2246.
39 J. Chen, K. Zou, P. Ding, J. Deng, C. Zha, Y. Hu, X. Zhao, J. Wu, J. Fan and Y. Li, *Adv. Mater.*, 2019, **31**, e1805484.
40 P. Tan, Z. H. Wei, W. Shyy, T. S. Zhao and X. B. Zhu, *Energy Environ. Sci.*, 2016, **9**, 1783–1793.
41 S. Yang, P. He and H. Zhou, *Energy Environ. Sci.*, 2016, **9**, 1650–1654.
42 J. Zhou, X. Li, C. Yang, Y. Li, K. Guo, J. Cheng, D. Yuan, C. Song, J. Lu and B. Wang, *Adv. Mater.*, 2019, **31**, 1804439.
43 Y. Li, J. Zhou, T. Zhang, T. Wang, X. Li, Y. Jia, J. Cheng, Q. Guan, E. Liu, H. Peng and B. Wang, *Adv. Funct. Mater.*, 2019, **29**, 1808117.
44 T. Jian, W. Ma, C. Xu, H. Liu and J. Wang, *eScience*, 2023, **3**, 100114.
45 Z. Wang, B. Liu, X. Yang, C. Zhao, P. Dong, X. Li, Y. Zhang, K. Doyle-Davis, X. Zeng, Y. Zhang and X. Sun, *Adv. Funct. Mater.*, 2023, **33**, 2213931.